Seismic behavior and modeling of steel reinforced concrete (SRC) walls

Article *in* Earthquake Engineering & Structural Dynamics · October 2014

DOI: 10.1002/eqe.2494

4 authors, including:

Xiaodong Ji
Tsinghua University
78 PUBLICATIONS **1,633** CITATIONS

Xinzheng Lu
Tsinghua University
316 PUBLICATIONS **8,014** CITATIONS

Xiaodong Ji, Ya Sun, Jiaru Qian, Xinzheng Lu. Seismic behavior and modeling of steel reinforced concrete (SRC) walls. *Earthquake Engineering and Structural Dynamics*, 2015, 44(6): 955-972.

Seismic Behavior and Modeling of Steel Reinforced Concrete (SRC) Walls

Xiaodong Ji, Ya Sun, Jiaru Qian and Xinzheng Lu

Department of Civil Engineering, Key Laboratory of Civil Engineering Safety and Durability of China Education Ministry, Tsinghua University, Beijing 100084, China

SUMMARY

The steel reinforced concrete (SRC) wall consists of structural steel embedded at the boundary elements of a reinforced concrete (RC) wall. The use of SRC walls has gained popularity in the construction of high-rise buildings because of their superior performance over conventional RC walls. This paper presents a series of quasi-static tests used to examine the behavior of SRC walls subjected to high axial force and lateral cyclic loading. The SRC wall specimens showed increased flexural strength and deformation capacity relative to their RC wall counterpart. The flexural strength of SRC walls was found to increase with increasing area ratio of embedded structural steel, while the section type of embedded steel did not affect the wall's strength. The SRC walls under high axial force ratio had an ultimate lateral drift ratio of approximately 1.4%. In addition, a multi-layer shell element model was developed for the SRC walls, and was implemented in the OpenSees program. The numerical model was validated through comparison with the test data. The model was able to predict the lateral stiffness, strength and deformation capacities of SRC walls with a reasonable level of accuracy. Finally, a number of issues for the design of SRC walls are discussed, along with a collection and analysis of the test data, including: (1) evaluation of flexural strength, (2) calculation of effective flexural stiffness, and (3) inelastic deformation capacity of SRC walls.

KEYWORDS: steel reinforced concrete (SRC) walls; seismic behavior; flexural strength; deformation capacity; multi-layer shell element model; axial force ratio

1. INTRODUCTION

Structural walls are widely used in building structures as the major structural members to provide substantial lateral strength, stiffness, and the inelastic deformation capacity needed to withstand earthquake ground motions. In recent years, steel reinforced concrete (SRC) walls have gained popularity for use in high-rise buildings in regions of high seismicity. SRC walls have additional structural steel embedded in the boundary elements of the reinforced concrete (RC) walls. The use of SRC walls offers the following potential advantages over conventional RC walls. (1) The embedded structural steel, acting in composite with the surrounding concrete, can increase both the flexural strength and shear strength of the walls. (2) Addition of structural steel at wall boundaries is expected to increase the deformation capacity and energy dissipation capacity of the walls when subjected to earthquake motions. (3) The embedded structural steel can enhance the stability of wall boundary elements and, therefore, effectively postpone or prevent the likely out-of-plane buckling failure of slender wall boundaries. (4) With the embedded steel, the wall piers are easily connected with the steel or SRC coupling beams that have seen increasing use in high-rise buildings.

In the past decade, great effort has been devoted to the study of seismic behavior of SRC

Please cite this article as: Xiaodong Ji, Ya Sun, Jiaru Qian, Xinzheng Lu. Seismic behavior and modeling of steel reinforced concrete (SRC) walls. Earthquake Engineering and Structural Dynamics, 2015, 44(6): 955-972. doi: 10.1002/eqe.2494

walls, for example, Wallace et al. [1], Dan et al. [2,3], and Qian et al. [4]. Design provisions for SRC walls have also been included in some leading design codes and specifications, for example, AISC 341-10 [5], Eurocode 8 [6], and JGJ 3-2010 [7]. However, most of the past tests involve SRC walls subjected to low axial force ratios and lateral cyclic loading. SRC walls used in the lower stories of high-rise buildings are usually subjected to high axial force ratios. Under increased axial force ratios, a level of ductility and deformation capacity significantly lower than those of the SRC walls featured in the past test data is anticipated. There is a clear need, therefore, to examine the seismic behavior on the SRC walls under high axial force ratios.

Another objective of this paper is to develop a high-fidelity numerical model for simulating SRC walls. Various types of numerical models have been developed for modeling RC walls, including the multiple-vertical-line-element model [8, 9], fiber beam-column models [10], and multi-layer shear element model [11, 12]. Of these, the multi-layer element model is found to offer a good compromise between computational efficiency and a reasonable level of accuracy. With modification, it is possible to extend this model to simulate SRC walls.

The next section of this paper will describe an experimental program in which six wall specimens were tested under high axial force and lateral cyclic loading. In the third section a multi-layer shell element model of a SRC wall based on the OpenSees program will be presented. Finally, in the fourth section, the design implications for SRC walls will be discussed in light of the results of the analysis of the test data.

2. EXPERIMENTAL TESTS

2.1. Experimental Program

2.1.1. Test specimens

The test specimens were designed to represent the lower story structural walls in high-rise buildings, and were fabricated at approximately one-third scale to accommodate the capacity of the loading facility. A total of six wall specimens were designed, including five SRC walls and one RC wall. The SRC wall specimens were labeled SRCW1 through SRCW5, and the RC wall specimen was labeled as RCW1. Fig. 1 shows the overall geometry of the specimens. The wall is 2550 mm tall and has an aspect ratio of approximately 2.3. A RC foundation beam with a cross-section of 350 mm by 500 mm and a RC top beam with a cross-section of 240 mm by 240 mm were cast together with the wall.

Fig. 2 shows the cross-sectional dimensions and reinforcing details of the wall specimens. All walls have a rectangular-shaped cross section with a depth of 1100 mm and a thickness of 140 mm. The shape and area ratio (i.e., the ratio of gross cross-sectional area of embedded steel to that of the boundary element) of the embedded steel section was taken as the variables of the SRC wall specimens. An I-profile steel beam was used for specimen SRCW1, a channel-profile steel beam for SRCW2 and SRCW3, square steel tubes for SRCW4, and circular steel tubes for SRCW5. Table 2 summarizes the dimensions of the embedded steel section and the area ratios of the steel for the specimens.

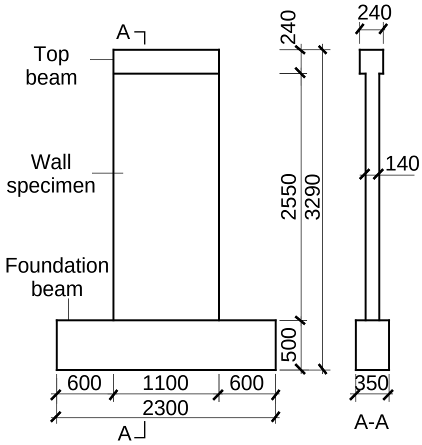

Figure 1. Elevation view of wall specimens (Unit: mm).

The wall specimens were designed to have the shear strength capacity of approximately 1.5 times the shear demand when the walls reach their flexural strength, ensuring the “strong shear and weak bending” mechanism. Six D12 (diameter = 12 mm) steel rebars were placed at the boundary elements as longitudinal reinforcement for all specimens, corresponding to a 2.2% reinforcement ratio (i.e., the ratio of gross cross-sectional area of longitudinal rebars to that of the boundary element). D8 (diameter = 8 mm) steel rebars were placed as distributed reinforcement at the wall web of the specimens. The spacing between the vertically distributed rebars was 120 mm for all specimens. The spacing between the horizontally distributed rebars for specimens SRCW1, SRCW4 and SRCW5 was 80 mm, while the spacing for SRCW2, SRCW3 and RCW1 was 100 mm. The boundary transverse reinforcement, made by D6 (diameter = 6 mm) steel rebars, was made in the form of rectangular hoops for all specimens. The vertical spacing of the boundary transverse reinforcement was 100mm for the bottom region of the walls, and 200 mm for the upper region of the walls, as shown in Fig. 2(h).

The embedded structural steel and vertical rebars were fully anchored into the foundation beam and top beam. Headed shear stud connectors were used for shear transfer between the embedded steel and surrounding concrete. The headed shear studs had a diameter of 8 mm and a length of 40 mm, and they were welded to the steel at vertical intervals of 100 mm.

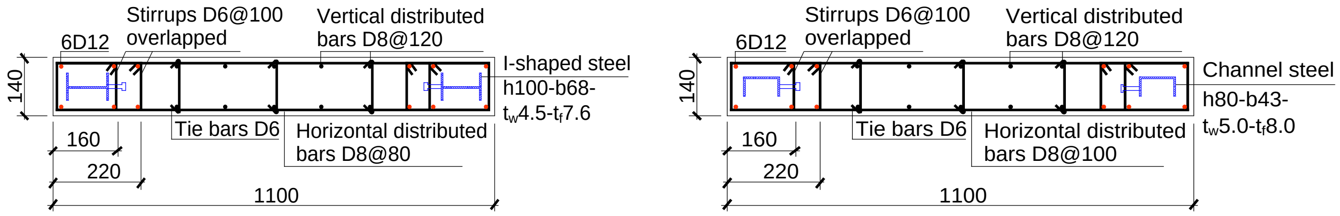

(a) SRCW1

(b) SRCW2

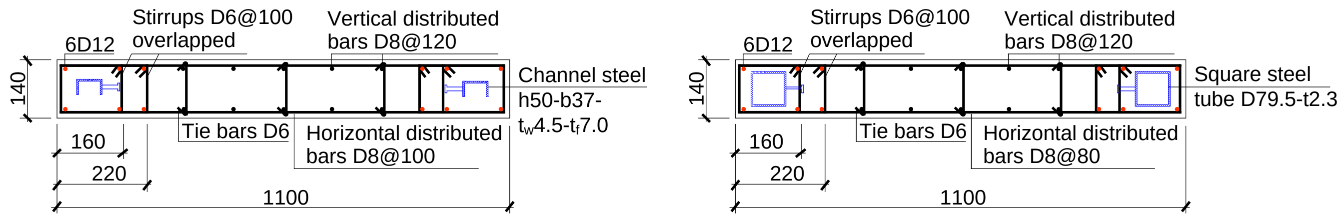

(c) SRCW3

(d) SRCW4

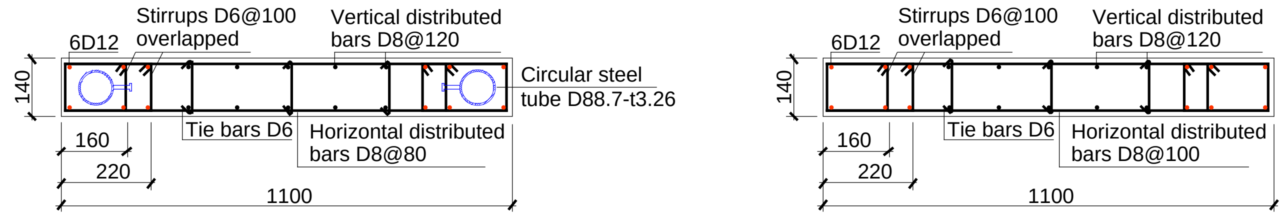

(e) SRCW5

(f) RCW1

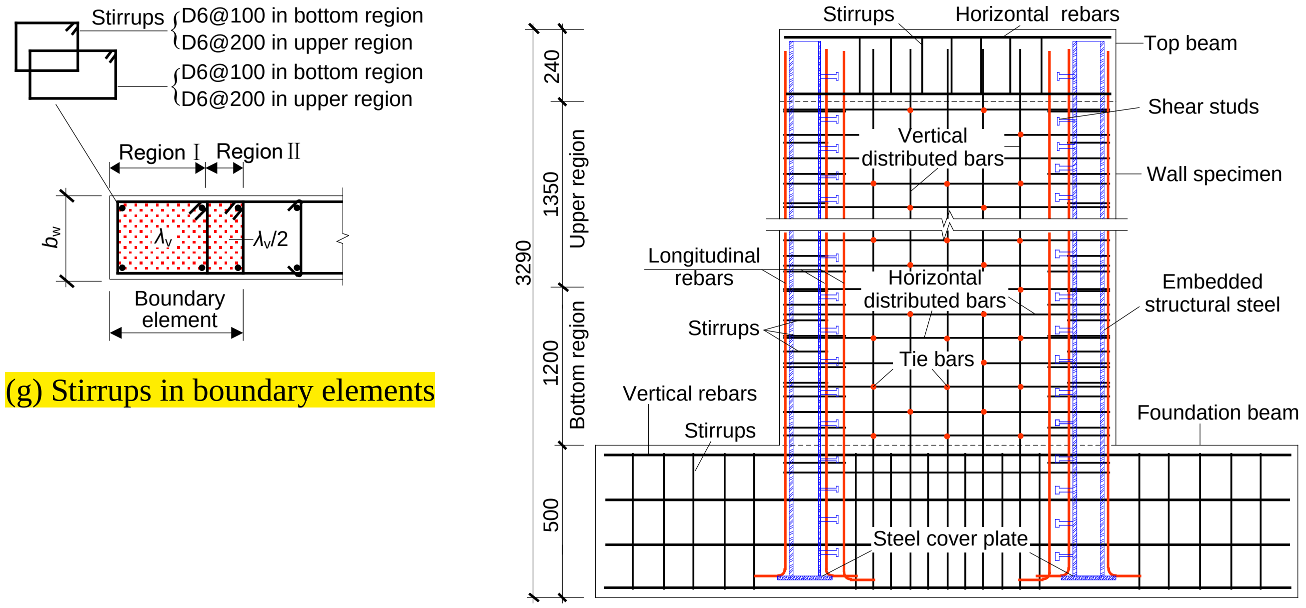

(g) Stirrups in boundary elements

(h) Elevation drawing of steel reinforcement

Figure 2. Dimensions and reinforcement details of wall specimens (Unit: mm).

The concrete used in the specimens has strength grade C40 (nominal cubic compressive strength $f_{\mathrm{cu,d}}$ = 40 MPa, and design value of axial compressive strength $f_{\mathrm{c,d}}$ =19.1 MPa). The actual cubic compressive strength $f_{\mathrm{cu,t}}$ of concrete was measured on cubes of 150 mm size and the results are listed in Table 1(a). Note that the actual value (named "test value" hereinafter) for the axial compressive strength of concrete $f_{\mathrm{c,t}}$ was taken as 0.76 $f_{\mathrm{cu,t}}$ in accordance with the Chinese Code for Design of Concrete Structures [13]. The D12 rebars were deformed steel bars with a strength grade of HRB335 (nominal yield strength f_y = 335 MPa), and the other rebars used in the specimens were plain steel bars with a strength grade of HPB235 (f_y = 235 MPa). The embedded structural steel had a strength grade of Q235 (f_y = 235 MPa). Table 1(b) summarizes the measured tensile yield strength $f_{\mathrm{y,t}}$ and ultimate strength $f_{\mathrm{u,t}}$ for the steel rebars and structural steel.

Table 1(a). Properties for concrete.

Specimen no.	Cubic compressive strength, $f_{cu,t}$ (MPa)	Axial compressive strength, $f_{c,t}$ (MPa)
SRCW1	43.4	33.0
SRCW2	42.8	32.5
SRCW3	45.0	34.2
SRCW4	41.3	31.4
SRCW5	37.1	28.2
RCW1	43.0	32.7

Table 1(b). Properties for steel.

Steel type	Yield strength, $f_{y,t}$ (MPa)	Ultimate strength, $f_{u,t}$ (MPa)
D6 rebar	418.7	586.7
D8 rebar	334.8	461.6
D12 rebar	375.5	554.1
I-profile steel	282.3	379.6
Channel-profile steel (h=50mm)	426.3	466.4
Channel-profile steel (h=80mm)	383.1	432.2
Rectangular tube	337.4	380.5
Circular tube	311.1	373.8

2.1.2. Design parameters

Aside from the shape and area ratio of the embedded steel section, the axial force ratio and the special boundary element are major consideration for the design of SRC walls.

The axial force ratio of SRC walls is defined as follows:

$$n = \frac{N}{f_c A_c + f_y A_s} \tag{1}$$

where N denotes the axial load applied on the wall; f_c and f_y denote the axial compressive strength of wall concrete and the yield strength of embedded steel, respectively; A_c and A_s denote the cross-sectional area of the concrete and the embedded steel, respectively.

Evaluating Eq. (1) with the design axial compressive load and the design values of the material strengths gives the design value of the axial force ratio, while using the actual axial load and the measured material strengths in Eq. (1) yields the test value (i.e., actual value) of the axial force ratio. A value of 1.2 was used for the load factor (i.e., the ratio of the design value of the axial load to the actual value), in accordance with the Chinese code for seismic design of buildings (GB 50011-2010) [14]. Allowing for both load factor and material strength reduction factor (i.e., the ratio of the design value of material strength to the test value), the design value of the axial force ratio is approximately 1.8 times the corresponding test value. Table 2 presents the axial force applied to the specimens and the corresponding axial force ratios. All specimens had similar axial force ratios, with a design value of approximately 0.58 and a test value of around 0.33. Note that GB 50011-2010 specifies the limit of the design axial force ratio as 0.6 for Seismic Grade II walls (ductile walls). The UBC code [15] specifies the limit of the axial force ratio $N/(A_c f_c^{'})$ as 0.35 for ductile walls, where the cylindrical compressive strength $f_c^{'}$ is used. In fact, taking into consideration the difference between the cylindrical compressive strength $f_c^{'}$ used in the UBC code and the design axial compressive strength f_c used in the Chinese code, the requirement for the wall's axial force ratio is similar in both codes.

GB 50011-2010 [14] requires that the extent of the special boundary element should be no less than 0.2 times the wall's cross-sectional depth for rectangular-shaped ductile walls under high axial force ratios. Therefore, the boundary elements of all specimens were designed to span 220 mm from the wall edge. Special transverse reinforcement was required for the boundary elements to confine the concrete and to delay the buckling of longitudinal rebars. The amount of transverse reinforcement is expressed in terms of the volumetric transverse reinforcement ratio ρ_v (i.e., the ratio of the volume of the stirrups to that of the concrete confined by stirrups) or the stirrup characteristic value λ_v specified in GB 50011-2010 (i.e., the mechanical volumetric ratio ω_{wd} specified in Eurocode 8 [6]). The stirrup characteristic value is defined as $\lambda_v = \rho_v f_{yv}/f_c$, where f_{yv} and f_c denote the yield strength of transverse reinforcement and the axial compressive strength of concrete, respectively. In GB 50011-2010 [14], the boundary element is divided into two regions, as shown in Fig. 2(g). Region I, which is at the edge of the wall, has double the transverse reinforcement of Region II. All specimens had a design stirrup characteristic value of over 0.2 for Region I, in accordance with the code requirement for ductile walls. Table 2 lists the design values and test values for the stirrup characteristic value in Region I.

Table 2. Design parameters of specimens.

Specimen no.	Embedded steel type	Dimension of steel (mm)	Area ratio ρ_a	Axial load (kN)	Axial force ratio		Stirrup characteristic value λ_v
					n_d	n_t	
SRCW1	I	h100-b_f68-t_w4.5-t_f7.6	3.60%	1700	0.57	0.32	0.25
SRCW2	[	h80-b_f43-t_w5.0-t_f8.0	2.56%	1700	0.58	0.32	0.26
SRCW3	[	h50-b_f37-t_w4.5-t_f7.0	1.74%	1750	0.58	0.32	0.24
SRCW4	□	b79.5-t2.3	2.31%	1700	0.58	0.34	0.26
SRCW5	○	D88.7-t3.3	2.84%	1450	0.57	0.32	0.29
RCW1	-	-	-	1700	0.60	0.34	0.25

Notes: (1) h, b_f, t_w and t_f represent the sectional height, flange width, web thickness and flange thickness, respectively; (3) the stirrup characteristic value λ_v is given for region I of the boundary element; (4) n_d and n_t represent the design value and test value of the axial force ratio, respectively.

2.1.3. Test setup, loading procedure, and instrumentation

The wall specimen was placed in a loading frame, as shown in Fig. 3. The foundation beam was securely clamped to the reaction floor. The top beam was clamped to two hydraulic actuators, one in the horizontal direction and another in the vertical direction. A rigid steel beam was placed between the wall's top beam and vertical actuator to distribute the vertical force uniformly across the wall section. The vertical actuator was free to move in the horizontal direction so as to accommodate the lateral deformation of the specimens. The vertical load was applied to the specimen at the beginning of the test and was maintained at a constant value for the duration of the test. Afterwards, lateral cyclic loads were applied quasi-statically by the horizontal actuator. The lateral loading point was 2670 mm above the base of the wall, and the shear-to-span ratio of the wall specimen was 2.43.

The lateral loading followed the protocol specified by the Chinese Specification of Testing Methods for Earthquake Resistant Building (JGJ 101-96) [16]. Before the specimen yielded, the lateral loading was force-controlled and one cycle was performed at each force level. Three levels were considered in this phase: 1/3, 2/3 and 1.0 times the predicted yield load $V_{y,p}$ of the specimen. After the specimen yielded, the loading was displacement-controlled and two cycles were repeated at each displacement level. The displacement loading amplitudes had an increment of $0.5\Delta_{y,p}$, where $\Delta_{y,p}$ denotes the predicted yield displacement of the specimen. In the test, push was defined as positive loading and pull as negative loading, and the order implemented was a push followed by a pull for each cycle. The test was terminated when the specimen lost its vertical load-carrying capacity due to compressive crushing of concrete at the base of the wall.

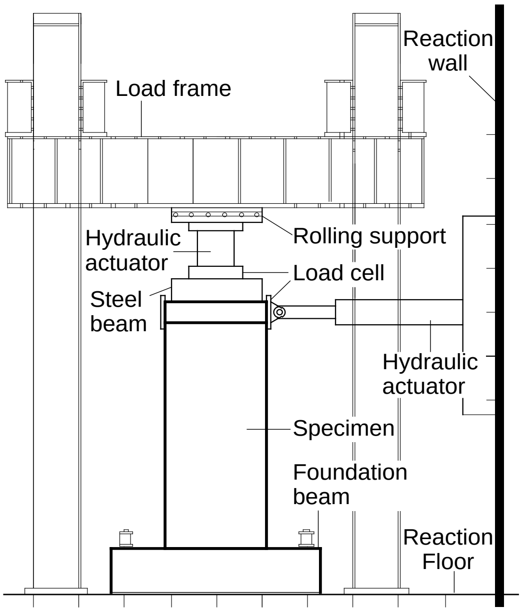

Figure 3. Test setup.

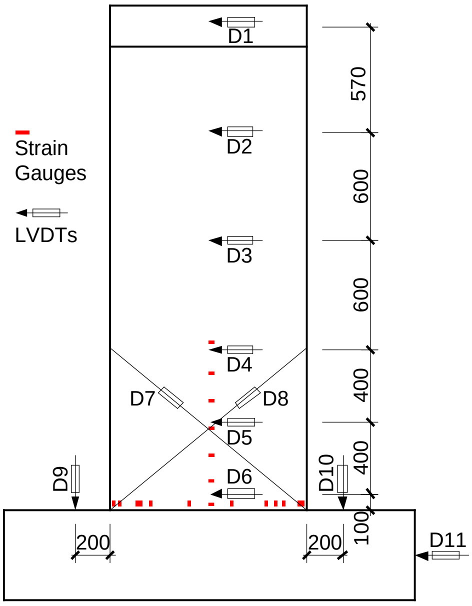

Figure 4. Specimen instrumentation.

Instruments were used to measure loads, displacements and strains of the specimen. Load cells measured the vertical and lateral loads applied to the specimen. Fig. 4 shows the locations of displacement transducers and strain gauges on the specimens. Six linear variable differential transformers (i.e., LVDTs D1 through D6) were used to measure the lateral displacements at various heights of the wall. A pair of crossed LVDTs (i.e., D7 and D8) measured the shear deformation of the base region of the wall. LVDTs D9 and D10 were used to monitor any rotation of the foundation beam, and D11 was used to monitor any slip of the foundation beam along the reaction floor. Strain gauges were mounted in the embedded structural steel and vertical rebars at approximately 20 mm above the wall base. The strains of the horizontally distributed rebars in the base region of the wall were also measured.

2.2. Experimental Results

The following presents the failure mode, hysteresis behavior, strength and deformation capacities. More details on energy dissipation capacity, strain, and strength and stiffness deterioration can be found in reference [17].

2.2.1. Failure mode

All specimens failed in a flexural mode. At approximately 0.15% lateral drift ratio, horizontal flexural cracks were initially observed at the base of the wall, in the tensile zone. As the drift increased, more horizontal cracks developed along the height of the wall. The horizontal cracks gradually propagated from the wall edge inwards, and then developed into inclined cracks. The longitudinal rebars and embedded steel yielded in compression at approximately 0.25% drift and yielded in tension at approximately 0.5% drift. The specimen reached its peak load at approximately 0.56% drift. Beyond this drift, vertical cracks caused by extremely large compressive strain occurred at the edges of the wall base. Concrete cover spalled off at further cycles. At approximately 1.3% drift, the longitudinal rebars in the boundary element buckled and the transverse rebars failed. As the drift continued to increase, significant crushing occurred in both boundary elements and the wall web, which led to complete failure of the wall.

Fig. 5 shows the concrete cracking and crushing of the wall specimens after testing. Fig. 6 shows the photographs of the specimens after testing, and Fig. 7 shows photographs of the boundary elements of the SRC walls post testing, after removal of concrete. Significant buckling of the longitudinal rebars and structural steel was observed at the base of the walls.

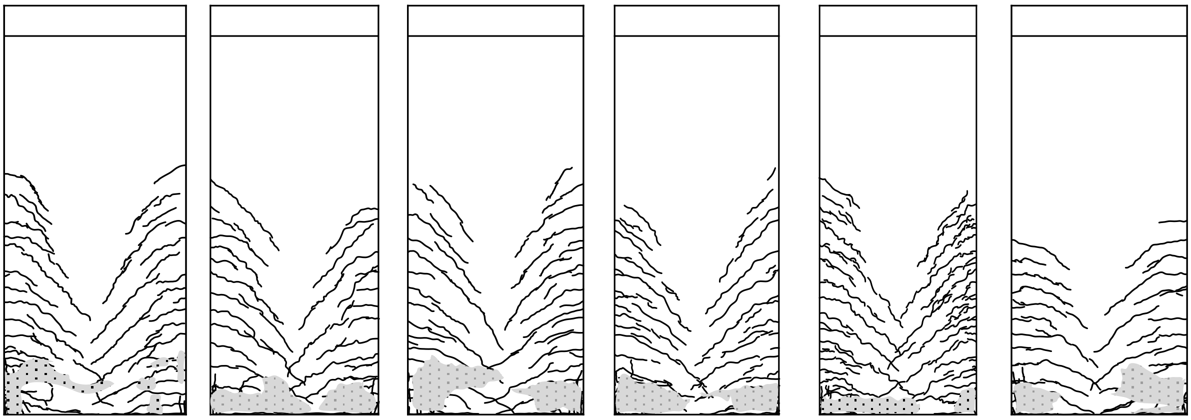

(a) SRCW1 (b) SRCW2 (c) SRCW3 (d) SRCW4 (e) SRCW5 (f) RCW1

Figure 5. Concrete cracking and crushing patterns of wall specimens after testing.

(a) SRCW1 (b) SRCW2 (c) SRCW3

(d) SRCW4 (e) SRCW5 (f) RCW1

Figure 6. Photographs of wall specimens after testing.

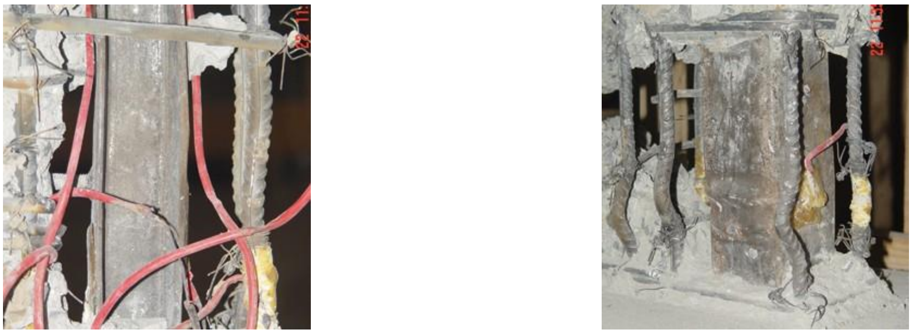

(a) SRCW3 (b) SRCW4

Figure 7. Photographs of boundary elements post testing, after removal of concrete.

2.2.2. Lateral force-displacement relationship

Fig. 8 shows the measured lateral force versus displacement relationships for all specimens. The hysteresis loops of the SRC wall specimens were full, demonstrating the inherent good energy dissipation capacity of SRC walls in flexural failure. The hysteresis loop of the RC wall was slightly pinched. Fig. 9 shows the envelope curves of the lateral force versus displacement relationships. All specimens had almost identical initial stiffness. The SRC wall specimens showed higher flexural strength than the RC wall. In addition, the SRC walls specimen exhibited slower strength deterioration after the peak loads compared to the RC wall.

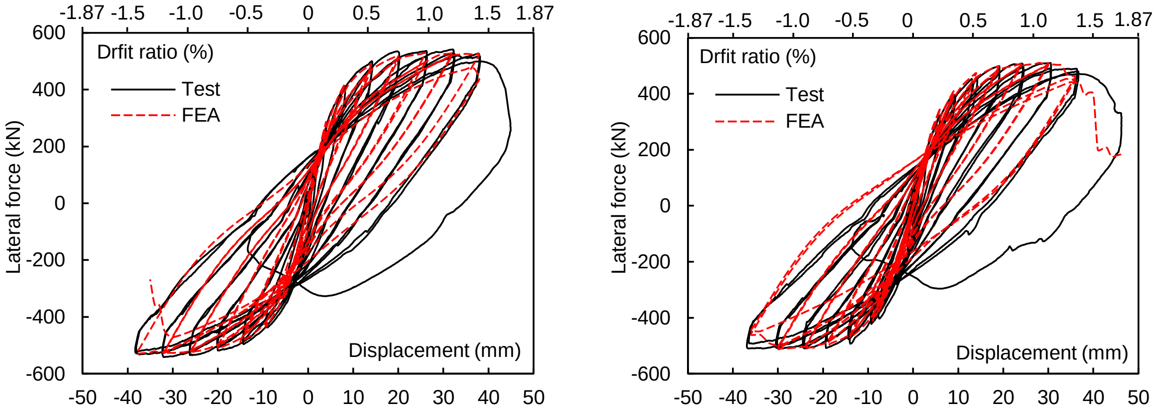

(a) SRCW1 (b) SRCW2

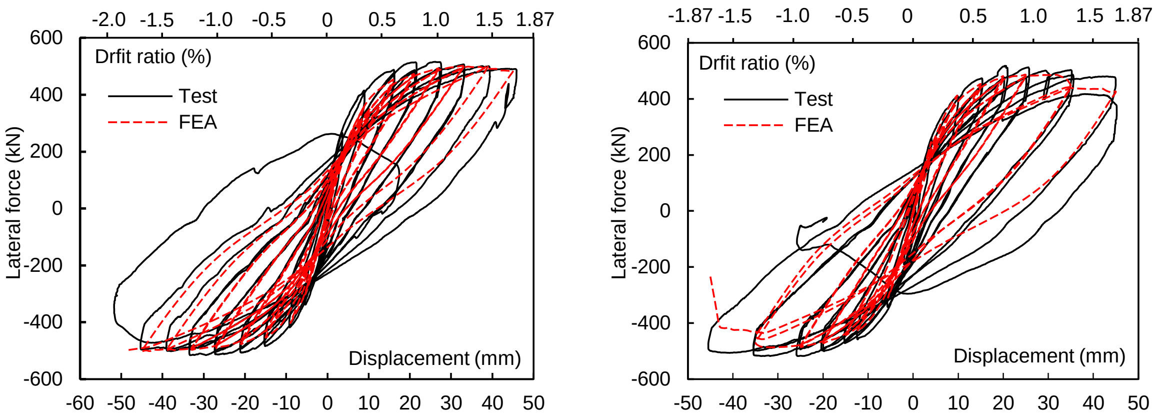

(c) SRCW3

(d) SRCW4

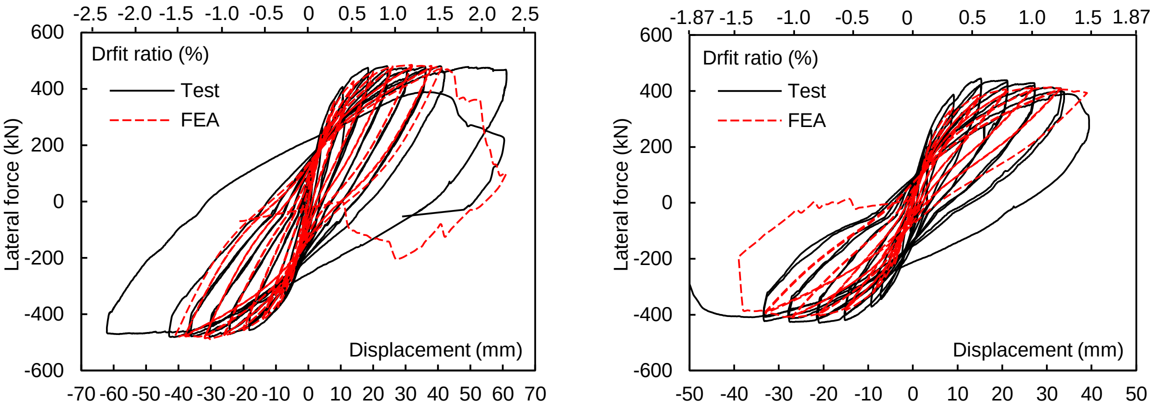

(e) SRCW5

(f) RCW1

Figure 8. Hysteresis loops for lateral force versus top displacement of specimens.

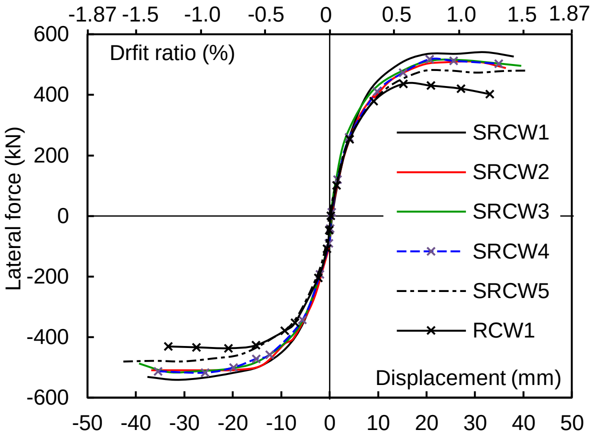

Figure 9. Envelope curves for lateral force versus top displacement of specimens.

2.2.3. Strength capacity

Table 3 shows the measured yield loads $V_{y,m}$ and peak loads $V_{p,m}$ of the specimens. The measured yield load $V_{y,m}$ was determined using the idealized force-displacement curve method specified in ASCE/SEI 41-06 [18]. The values shown in Table 3 are the average values of the loads measured in the push and pull directions. Specimens SRCW2 through

SRCW5, which had similar area ratios of embedded steel, had nearly identical yield loads and peak loads. The sectional type of embedded steel appeared to make no difference to the strength capacity of the SRC wall specimens. Specimen SRCW1, which had a higher area ratio of embedded steel than other SRC wall specimens, had an increased yield load and peak load. Due to the addition of the embedded steel, the SRC wall specimens showed an increased flexural strength when compared with the RC wall. The peak loads of specimens SRCW2 through SRCW5 were on average 15.8% higher than that of RCW1, and the peak load of Specimen SRCW1 was 23.9% higher than that of RCW1.

Table 3. Lateral load-carrying capacity of specimens.

Specimen no.	Area ratio of embedded steel ρ_a	Measured yield load $V_{y,m}$ (kN)	Measured Peak load $V_{p,m}$ (kN)
SRCW1	3.60%	439.7	541.3
SRCW2	2.56%	405.6	509.6
SRCW3	1.74%	400.4	515.4
SRCW4	2.31%	405.2	517.9
SRCW5	2.84%	390.7	480.8
RCW1	-	356.0	436.9

2.2.4. Deformation capacity

Table 4 summarizes the measured yield displacement Δ_y, ultimate displacement Δ_u, ultimate drift ratio θ_u, and displacement ductility ratio μ_Δ of the specimens. The yield displacement Δ_y corresponds to the measured yield load $V_{y,m}$. The ultimate displacement Δ_u for a SRC wall is usually defined as the post-peak displacement at the instant when the lateral load has decreased to 85% of its peak value. In this test, the specimens did not show obvious degradation of lateral load-carrying capacity until complete failure, which was induced by a loss of the vertical loading-carrying capacity. Therefore, the ultimate displacement Δ_u was defined as the maximum displacement that the specimen endured before the cycle of complete failure [4]. Note that the values in Table 4 are the average values of the displacements measured in the push and pull directions. The ultimate drift ratio θ_u was calculated as $\theta_u = \Delta_u/H$, where H denotes the height of the central axis of the horizontal actuator, relative to the wall base. The displacement ductility ratio μ_Δ was calculated as $\mu_\Delta = \Delta_u/\Delta_y$.

The SRC specimens had an increased ultimate drift ratio relative to the RC wall. Although specimen SRCW1 had a higher area ratio of embedded steel than the other SRC wall specimens, this made no obvious difference to the ultimate drift ratio. Interestingly, specimen SRCW5 had an ultimate drift approximately 15% higher than any of the other SRC specimens, which might be attributable to the confinement of the infilled concrete provided by the circular steel tube. The ductility ratio μ_Δ of the wall specimens was around 5.0. The ductility ratio of the SRC specimens was similar to that of the RC wall because the addition of embedded steel led to an increase in both the ultimate displacement and the yield displacement.

Table 4. Deformation capacity and ductility ratio of specimens.

Specimen no.	Area ratio of embedded steel ρ_a	Yield disp. $\varDelta_y$ (mm)	Ultimate disp. $\varDelta_u$ (mm)	Ultimate drift ratio θ_u	Disp. ductility ratio μ_Δ
SRCW1	3.60%	7.75	38.23	1.43%	4.9
SRCW2	2.56%	6.92	36.79	1.38%	5.3
SRCW3	1.74%	6.83	39.22	1.47%	5.7
SRCW4	2.31%	7.67	35.52	1.33%	4.6
SRCW5	2.84%	7.00	42.51	1.59%	6.1
RCW1	-	6.83	33.66	1.26%	4.9

2.2.5. Strains

Fig. 10 shows the vertical strain profiles of the wall bottom section for Specimen SRCW3 at various drift levers. The data were obtained from the strain gauges mounted on the embedded steel and longitudinal rebars. At 0.5% drift, the wall section had a linear strain profile. Since the wall subjected to high compressive force, the strain in the compression edge was large than the tensile strain in the tension edge. After 1.0% drift, large plastic strains concentrated at the wall's compression edge, which was consistent to the test observation of spalling of concrete cover and buckling of steel and rebars. At 1.5% drift where the specimen failed, the compressive strain developed in the embedded steel was over 0.02. In addition, the strain data indicate that the stresses of horizontally distributed rebars did not exceed their yield strength until the final failure stage.

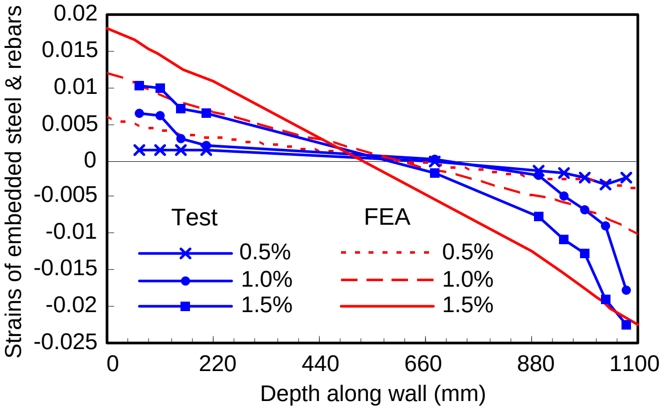

Figure 10. Vertical strain profiles of SRCW3.

3. NUMERICAL MODEL OF SRC WALLS

3.1. Multi-layer shell element

The multi-layer shell element consists of a number of concrete layers and rebar layers [11,12]. Fig. 11 shows a sketch of a multi-layer shell element used for modeling RC walls. The concrete cover and inside concrete are represented by a number of concrete layers, and the distributed reinforcements are represented by the smeared rebar layers in vertical and horizontal directions, respectively. It has been proved that the multi-layer shell element for modeling RC walls can ensure both computational efficiency and reasonable level of accuracy [12]. Recently, Xie et al. [19, 20] have implemented the multi-layer shell element in the computation platform OpenSees for modeling RC walls. In this paper, a model using the multi-layer shell element will be extended for modeling SRC walls.

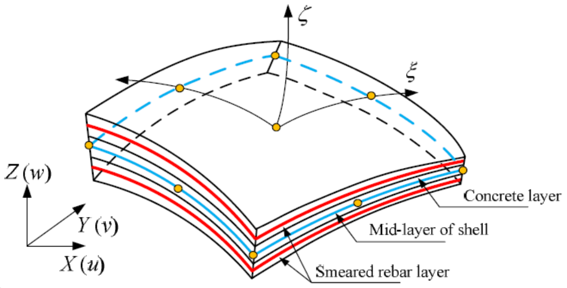

(a) Multi-layer shell element

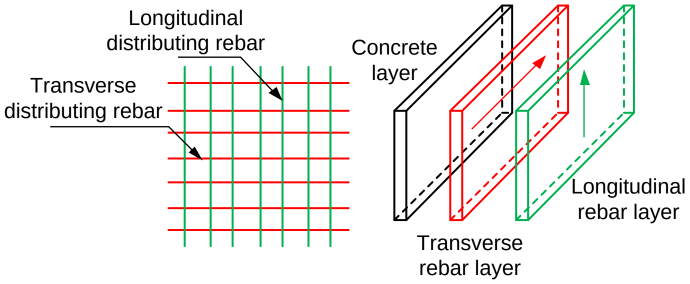

(b) Location of the rebar layers

Figure 11. Sketch of multi-layer shell element for RC wall [12].

3.2. Materials

3.2.1. Concrete

Well-calibrated concrete models were adopted to represent the uniaxial stress-strain relationship of the concrete. The Kent-Park model [21] was used to represent the compressive uniaxial stress-strain relationship of the concrete cover, where the peak strain and spalling strain were assumed to be 0.002 and 0.005, respectively, and the post-spalling strength was taken as zero. The stirrup-confined concrete was represented by the Saatcioglu-Razvi model [22], which takes into account the increase of the strength and ductility of concrete due to the confinement effect. The residual compressive strength after ultimate strain was taken to be 0.2 times the peak strength of the concrete. A model proposed by Susantha et al. [23] was used for the infilled concrete confined by steel tubes. Fig. 12(a) shows the uniaxial compressive stress-strain relationship curves for the concrete of specimen SRCW1. A bilinear stress-strain curve with tension softening was adopted to represent the tensile behavior of the concrete. The tensile strength of the concrete was taken as 10% of its peak compressive strength, and the ultimate tensile strain was assumed to be 0.001. Fig. 12(b) shows the hysteresis curve used to represent the cyclic behavior of the concrete. Allowing for computational efficiency and convergence, an origin-oriented linear curve was used for the unloading path, which might induce additional pinching in the analysis results.

The concrete behaved in a plane-stress manner in the multi-layer shell element. The nonlinearity of the concrete was expressed based on the concept of damage mechanics. The constitutive equation of concrete in a state of planar stress was given by:

$$\boldsymbol{\sigma}_{\mathrm{c}}' = \begin{bmatrix} 1-d_1 & \\ & 1-d_2 \end{bmatrix} \boldsymbol{D}_{\mathrm{e}} \boldsymbol{\varepsilon}_{\mathrm{c}}' \tag{2}$$

where $\boldsymbol{\sigma}_{\mathrm{c}}'$ and $\boldsymbol{\varepsilon}_{\mathrm{c}}'$ represent the stress and strain tensors, respectively, in the principal stress coordinate system before cracking and in the crack coordinate system after cracking; $\boldsymbol{D}_{\mathrm{e}}$ is the elastic constitutive matrix; and d_1 and d_2 are the damage parameters, which can be determined by the damage evolution curves for concrete under tension from Løland [24] and for concrete under compression from Mazars [25].

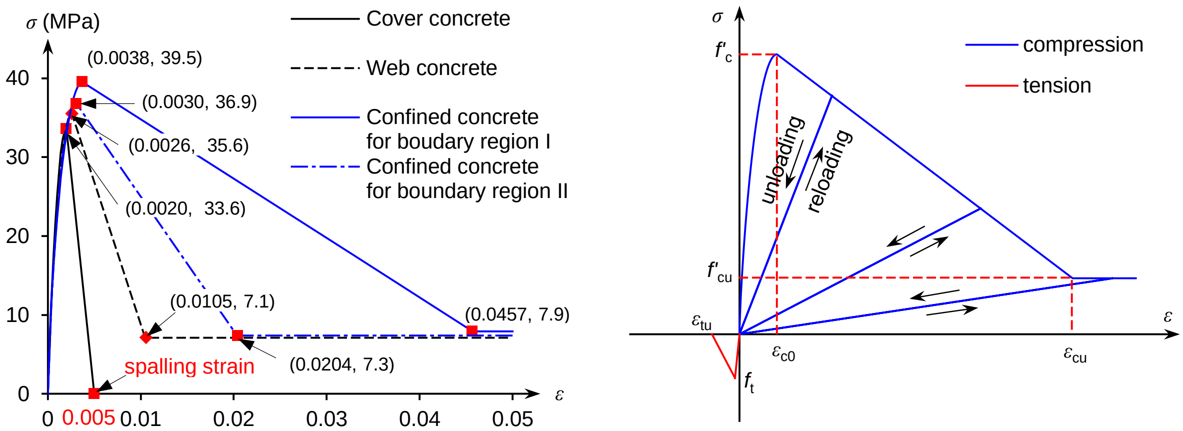

(a) uniaxial stress-strain relationship curve for the concrete of specimen SRCW1

(b) stress-strain relationship curve for concrete under cyclic loading

Figure 12. Concrete model.

The cracking of concrete was modeled by the fixed smeared crack approach. Cracks were assumed to occur when the principal tensile stress exceeded the specified concrete tensile strength. After cracking, concrete was treated as an orthotropic material. The reduced shear stiffness for post-cracking concrete was taken to be the product of the elastic shear modulus G and the shear retention factor η. Therefore, the relationship between shear stress τ and shear strain γ for post-cracking concrete in the crack coordinate system can be written as:

$$\tau = \eta \cdot G \cdot \gamma \qquad (0 < \eta < 1.0) \tag{3}$$

The recommended value for the shear retention factor η was 0.1 in the nonlinear analysis of RC shear walls by Ile and Reynouard [26]. In this study, a value of 0.13 was used for η, as determined by trial-and-error.

3.2.2. Steel

The Giuffre-Menegotto-Pinto steel model [27, 28] was adopted for the uniaxial stress-strain relationship of the structural steel and rebars. Fig. 13 shows the uniaxial stress-strain relationship curve for steel. The values for yield strength f_y and Young's modulus E_0 were determined from the tensile coupon tests for steel. The strain-hardening ratio, which denotes the ratio of post-yielding stiffness to the initial stiffness, was taken as 1%. The parameters R_0, cR_1 and cR_2, which control the curve shape of the transition from elastic to plastic branches, were taken as 18.5, 0.925 and 0.15, respectively, in accordance with the recommendations made by Taucer [28].

Although the distributed rebars were represented by smeared rebar layers, the vertical rebars and horizontal rebars were defined separately in the two perpendicular directions in those layers. Therefore, the plane-stress state was simplified to a uniaxial stress state in two directions.

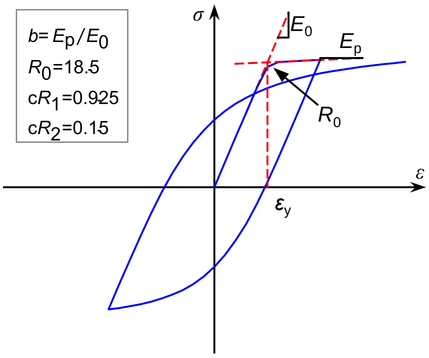

Figure 13. Cyclic stress-strain curve for steel.

3.3. Section, elements, mesh and loading

The sections of wall specimens were classified into three categories: RC wall (i.e., RCW1, see Fig. 14(a)), the walls embedded with shaped steel (i.e., SRCW1, SRCW2 and SRCW3, see Fig. 14(b)), and the walls embedded with steel tubes (i.e., SRCW4 and SRCW5, see Fig. 14(c)). The concrete and distributed rebars were modeled with the multi-layer shell elements. The longitudinal rebars in boundary elements were modeled with truss elements. Note that two longitudinal rebars at the same distance were condensed into one truss element for simplicity. The shaped steel and steel tubes were represented by a number of truss elements (see Fig. 14(b) and (c)).

Since the confinement effect on the concrete by the transverse reinforcement varied for the wall web, region II at the boundary element, and Region I at the boundary element, different uniaxial stress-strain relationships for the concrete were used, an example of which is shown in Fig. 12(a) for specimen SRCW1. In addition, the Susantha model, which took into account the confinement by the steel tube [23], was used to represent the infilled concrete.

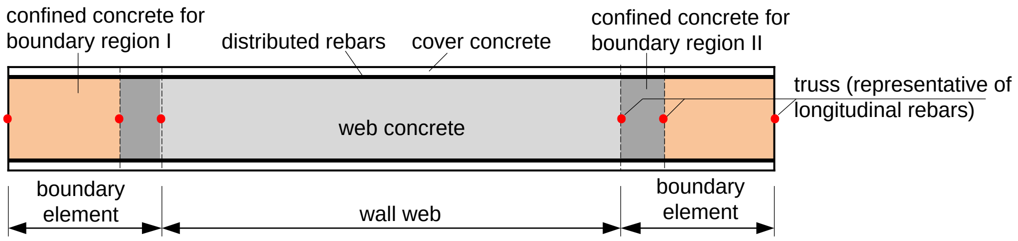

(a) RC wall

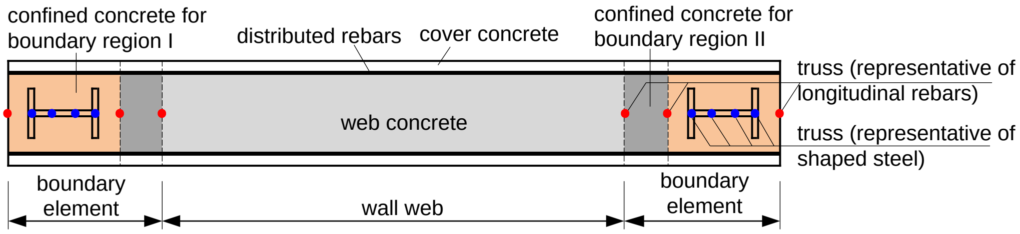

(b) SRC walls embedded with shaped steel

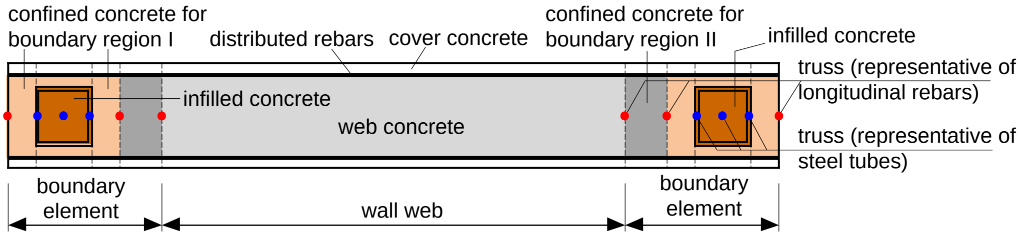

(c) SRC walls embedded with steel tubes

Figure 14. Sections of wall specimens.

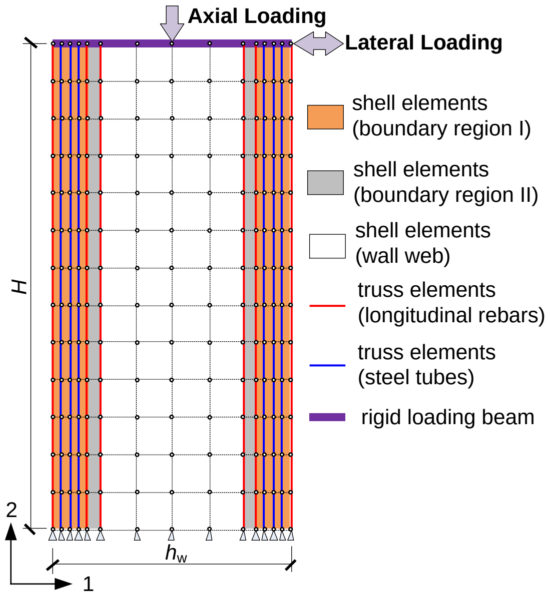

Figure 15. Finite element mesh and boundary conditions for SRCW4.

Fig. 15 shows the element mesh for the SRC walls. The truss elements were coupled with the surrounding shell elements at the common nodes. A suitable mesh size was determined after trialing various different mesh sizes.

All DOF of nodes at the base of the walls were fully fixed. A rigid beam was placed on the wall's top to mimic the loading beam of the wall specimens. The vertical load and lateral cyclic loads were applied to the wall through the rigid beam.

3.4. Comparison between numerical prediction and test results

Fig. 8 compares the wall's hysteresis curves from the numerical analysis with the test results. The numerical analysis tracked the test data well, even at the severe inelastic stage.

Table 5 lists the comparison of effective lateral stiffness, peak load, and ultimate displacement. The effective lateral stiffness was determined in according with ASCE/SEI 41-06 [18]. The numerical analysis underestimated the effective lateral stiffness of the wall specimens by 8.3% on average but accurately predicted the peak lateral load, with an average error of only 2.6%. The predicted ultimate displacement was also consistent with the test results. The errors for displacement predictions were less than 5% in all cases except for specimen SRCW1. Note that, the ultimate displacement in numerical analysis was defined as the lateral displacement before the last loading cycle where the computation stopped because of the numerical instability induced by the concrete failure.

Table 5. Comparison between numerical prediction and test results.

Specimen No.		SRCW1	SRCW2	SRCW3	SRCW4	SRCW5	RCW1	Ave.
Effective stiffness (kN/mm)	Test	64.7	68.2	73.8	64.8	63.8	62.5	
	Numerical	68.5	62.8	58.1	59.7	58.0	56.7	
	Error (%)	5.8	-8.0	-21.3	-7.9	-9.2	-9.2	-8.3
Peak load (kN)	Test	541.2	509.8	516.1	517.9	480.9	436.9	
	Numerical	528.3	510.3	502.7	486.1	486.3	411.6	
	Error (%)	-2.4	0.1	-2.6	-6.1	1.1	-5.8	-2.6
Ultimate displacement (mm)	Test	38.0	36.0	40.0	35.0	43.0	33.0	
	Numerical	32.0	36.0	40.0	35.0	41.0	33.0	
	Error (%)	15.8	0.0	0.0	0.0	-4.7	0.0	-3.4

Fig. 10 compares the strain values obtained from the numerical analysis with the test data. At 0.5% drift, the predicted strain values correlated well with the test results. After 1.0% drift, some discrepancies were observed between the predicted strains and test data. In general, the tensile strain values from the numerical analysis were larger than the test data, which can be explained by the following discussion. The test strain data were measured by strain gauges mounted on the embedded steel and rebars. The tensile strains at a section between concrete cracks can be smaller than the strains at the section of concrete cracking. Occasionally, the strain gauges at the wall base had not been across concrete cracks in this test. While the numerical model used the smear crack approach, which gave an average tensile strain of the steel or rebar along the element. In addition, the predicted strain values for the horizontal distributed rebars could track the trend of the strain data observed from the experimental tests.

4. DESIGN IMPLICATION

4.1. Flexural strength evaluation

In design, the flexural strength of SRC walls is usually calculated using a handy program for cross section analysis, for example XTRACT [29]. The XTRACT program is based on a fiber model, where each fiber follows the uniaxial stress-strain relationship of materials and the fiber's strain distribution satisfies the assumption that the plane section remains plane after bending. In the following analysis, the concrete used the uniaxial stress-strain relationships similar to those specified in subsection 3.2. The uniaxial stress-strain relationships of the steel were represented by a bilinear model, where the strain-hardening ratio was assumed to be 2.5% as recommended by Orakcal and Wallace [30].

Fig. 16 shows the evaluated flexural strengths of the wall specimens by XTRACT, compared with the test results. Note that the flexural strength corresponded to the failure section of the wall specimen, which was approximately 150 mm higher than the wall base. The evaluated strength and test data for the SRC wall specimens in the studies of Dan et al. [2] and Qian et al. [4] are also shown in the figure. Note that the SRC walls in Dan et al. correspond to a low axial force ratio of approximately 0.02, and the walls in Qian et al. had a relatively high axial force ratio of 0.29 to 0.38. The cross section analysis by XTRACT provides a relatively accurate estimation of the flexural strength of SRC walls, with the error of 4.6% relative to the test values on average.

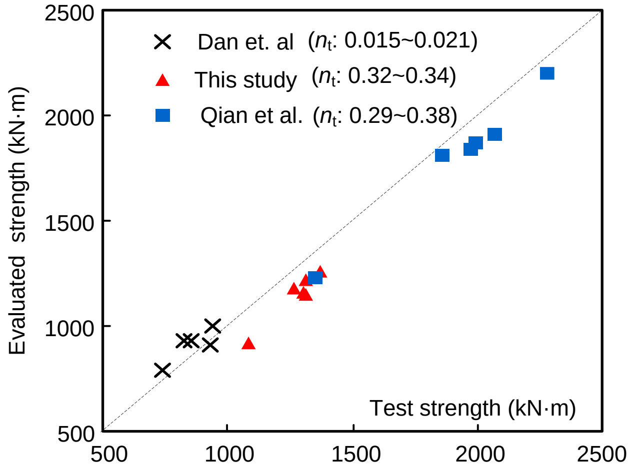

Figure 16. Comparison between evaluated flexural strength and test results.

4.2. Effective flexural stiffness

Effective flexural stiffness of the walls is a key modeling parameter that has a significant effect on the system response in structural analysis. The effective flexural stiffness is smaller than the gross flexural stiffness, which reflects the influence of concrete cracking and bond slippage. For RC walls, ASCE/SEI 41-06 specifies the effective flexural stiffness EI_{eff} as $0.5EI_{\mathrm{g}}$ for cracked RC walls and $0.8EI_{\mathrm{g}}$ for uncracked RC walls [18], where EI_{g} denotes the gross flexural stiffness of the wall section. Adebar et al. recommends the upper- and lower-bounds for the flexural stiffness shown in equation (4), which takes into account the effect of axial force ratio [31, 10]. This equation has been adopted by the Canadian Code.

$$EI_{\mathrm{eff}} = \begin{cases} (0.6+n)EI_{\mathrm{g}} \le EI_{\mathrm{g}}, & \text{Upper-bound} \\ (0.2+2.5n)EI_{\mathrm{g}} \le 0.7EI_{\mathrm{g}}, & \text{Lower-bound} \end{cases} \tag{4}$$

Similarly, the effective flexural stiffness of SRC walls is assumed to be smaller than the initial stiffness of wall section. The effective flexural stiffness of the SRC wall specimens can be calculated with the measured effective lateral stiffness of the SRC walls by assuming that the walls behave as cantilevers. Fig. 17 shows the effective flexural stiffness of the SRC wall specimens normalized with the gross flexural stiffness $EI_g = E_cI_c + E_sI_s$, where E_cI_c denotes the flexural stiffness of the concrete and E_sI_s denotes the flexural stiffness of the embedded steel about the sectional centroid. The values of effective flexural stiffness for SRC walls significantly increased along with an increase in the axial force ratio. For the SRC walls under high level of axial force ratios, the effective flexural stiffness values fell into the range between the upper-bound and lower-bound values recommended by Adebar et al. While the effective flexural stiffness values of the SRC walls under low level of axial force ratios were slightly smaller than the lower-bound value. In general, the lower-bound value of the effective flexural stiffness recommended by Adebar et al. had good agreement with the test results. Nevertheless, further validation is needed because there is still a lack of test data for SRC walls under moderate axial force ratios.

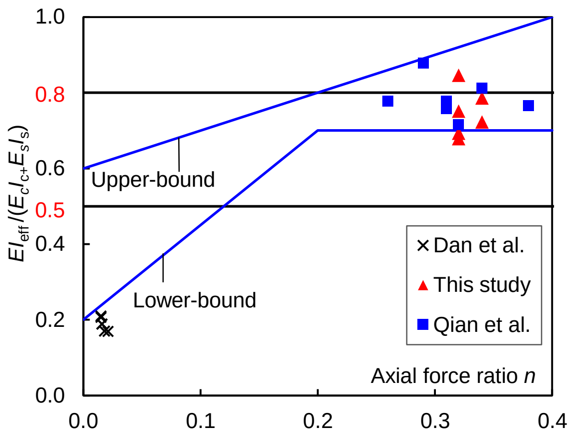

Figure 17. Effective flexural stiffness versus axial force ratio.

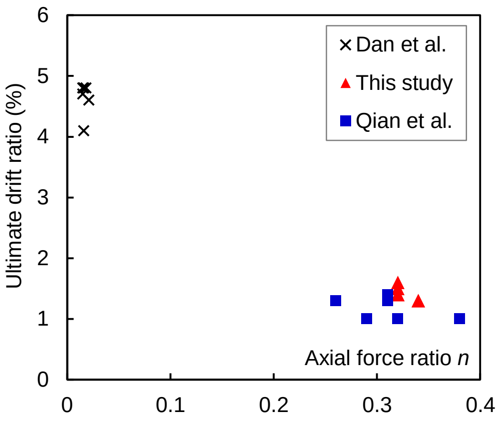

Figure 18. Ultimate drift ratio versus axial force ratio.

4.3. Inelastic deformation capacity

Fig. 18 summarizes the test data for the ultimate drift ratios of SRC walls under various axial force ratios. The SRC walls under low axial force ratios had an ultimate drift ratio of around 4.5%, while the walls under high axial force ratio had an ultimate drift ratio of approximately 1.4%. An increase of axial force ratio could significantly decrease the inelastic deformation capacity of SRC walls. Chinese code GB 50011-2010 requires that the inelastic deformation capacity be no less than 1.0% for structural walls. Even under high axial force ratios, the SRC walls could satisfy this requirement. Note that the extent of boundary elements and the amount of boundary transverse reinforcement also influences the wall's inelastic deformation capacity. The SRC wall specimens in Dan et al. [2], and Qian et al. [4] were found to satisfy the design provisions on special boundary elements of ductile walls required by GB

50011-2010.

5. CONCLUSIONS

This paper presents a series of quasi-static tests to examine the seismic behavior of SRC walls under high axial force ratios. A high-fidelity numerical model was developed for SRC wall simulation. The following conclusions and design recommendations are drawn from this study.

(1) The SRC wall specimens had higher flexural strength than the RC wall. The flexural strength increased with an increase in the area ratio of embedded structural steel, while the section type of embedded steel made no difference to the flexural strength of the SRC walls.

(2) The SRC wall specimens showed increased ultimate lateral drift when compared to the RC wall. The SRC walls under high axial force ratios had an ultimate lateral drift ratio of approximately 1.4%. Among the SRC walls, the wall embedded with circular steel tubes showed the largest deformation capacity.

(3) A multi-layer shell element model was developed for SRC wall simulation in the computation platform OpenSees. The numerical model was able to predict the lateral force-displacement hysteresis loops of the SRC walls with a reasonable level of accuracy. The lateral stiffness, strength and deformation capacities of the SRC walls obtained by numerical analysis correlated well with the test results.

(4) The cross section analysis provided a relatively accurate estimation of the flexural strength of the SRC walls.

(5) The effective flexure stiffness of SRC walls is highly dependent on the applied axial force ratio. The recommendation for effective flexural stiffness of RC walls specified by Adebar et al. appeared to be appropriate for use in calculation of the effective flexural stiffness of SRC walls under high axial force ratios.

ACKNOWLEDGMENTS

The work presented in this paper was sponsored by the International Science & Technology Cooperation Program of China (Grant No. 2014DFA70950), the National Natural Science Foundation of China (Grants No. 51261120377 and No. 91315301) and Tsinghua University Initiative Scientific Research Program (Grant No. 2012THZ02-1). The writers wish to express their sincere gratitude to the sponsors.

REFERENCES

[1] Wallace JW, Orakcal K, Cherlin M, Sayre BL. Lateral-load behavior of shear walls with structural steel boundary columns. *Proceedings of sixth ASCCS Conference on Composite and Hybrid Structures.* Los Angeles, USA, 2000: 801-808.

[2] Dan D, Fabian A, Stoian V. Theoretical and experimental study on composite steel–concrete shear walls with vertical steel encased profiles. *Journal of Constructional Steel Research* 2011; **67**(5): 800-813.

[3] Dan D, Fabian A, Stoian V. Nonlinear behavior of composite shear walls with vertical steel encased profiles. *Engineering Structures* 2011; **33**(10): 2794-2804.

[4] Qian J, Jiang Z, Ji X. Behavior of steel tube-reinforced concrete composite walls subjected to high axial force and cyclic loading. *Engineering Structures* 2012; **36**: 173-184.

[5] AISC. *Seismic provisions for structural steel buildings (ANSI/AISC Standard 341-10)*. American Institute of Steel Construction: Chicago, 2010.

[6] CEN. *EuroCode 8: Design Provisions for Earthquake Resistance-Part 1: General Rules, Seismic Actions and Rules for Buildings*. European Committee for Standardization: Brussels, 2004.

[7] CMC. *Technical specification for concrete structures of tall building (JGJ 3-2010).* China Ministry of Construction: Beijing, 2011 (in Chinese).

[8] Vulcano A, Bertero VV, Colotti V. Analytical modeling of R/C structural walls. *Proceedings, 9th world conference on earthquake engineering* 1988; **6**: 41-6.

[9] Orakcal K, Wallace JW, Conte JP. Flexural modeling of reinforced concrete walls-model attributes. *ACI Structural Journal* 2004; **103**(2): 196-206.

[10] PEER/ATC. Modeling and acceptance criteria for seismic design and analysis of tall buildings, PEER/ATC 72-1 Report, Applied Technology Council, Redwood City, CA, October 2010.

[11] Miao Z, Ye L, Guan H, Lu X. Evaluation of modal and traditional pushover analyses in frame-shear-wall structures. *Advances in Structural Engineering* 2011; **14**(5): 815-836.

[12] Lu X, Lu X, Guan H, Ye L. Collapse simulation of reinforced concrete high-rise building induced by extreme earthquakes. *Earthquake Engineering and Structural Dynamics* 2013; **42**(5): 705-723.

[13] CMC. *Code for Design of Concrete Structures (GB 50010-2010).* China Ministry of Construction: Beijing, 2010 (in Chinese).

[14] CMC. *Code for Seismic Design of Buildings (GB 50011-2010).* China Ministry of Construction: Beijing, 2010 (in Chinese).

[15] ICBO. *Uniform Building Code.* International Conference of Building Officials: Whittier, California, 1997.

[16] CMC. *Specification of testing methods for earthquake resistant building (JGJ 101-96).* Beijing: China Planning Press, 1997 (In Chinese).

[17] Qian J, Wei Y, Zhao Z, Cai Y, Yu Y, Shen L. Experimental study on seismic behavior of SRC shear walls with high axial force ratio. *Journal of Building Structures* 2008; **29**(2): 43-50 (in Chinese).

[18] ASCE/SEI Seismic Rehabilitation Standards Committee. *Seismic Rehabilitation of Existing Buildings (ASCE/SEI 41-06).* American Society of Civil Engineers: Reston, Virginia, 2007.

[19] Xie LL, Huang YL, Lu XZ, Lin KQ Ye LP. Elasto-plastic analysis for super tall RC frame-core tube structures based on OpenSees. *Engineering Mechanics* 2014; **31**(1): 64-71 (in Chinese).

[20] OpenSees Wiki: NDMaterial Command -- Materials for Modeling Concrete Walls. http://opensees.berkeley.edu/wiki/index.php/NDMaterial_Command.

[21] Kent DC, Park R. Flexural members with confined concrete. *Journal of the Structural Division* 1971; **97**(7): 1969-1990.

[22] Saatcioglu M, Razvi SR. Strength and ductility of confined concrete. *Journal of Structural Engineering (ASCE)* 1992; **118**(6): 1590-1607.

[23] Susantha KAS, Ge H, Usami T. Uniaxial stress–strain relationship of concrete confined by various shaped steel tubes. *Engineering Structures* 2001; **23**(10): 1331-1347.

[24] Løland KE. Continuous damage model for load-response estimation of concrete. *Cement and Concrete Research* 1980; **10**(3): 395-402.

[25] Mazars J. A description of micro- and macroscale damage of concrete structures. *Engineering Fracture Mechanics* 1986; **25**(5): 729-737.

[26] Ile N, Reynouard JM. Nonlinear analysis of reinforced concrete shear wall under earthquake loading. *Journal of Earthquake Engineering* 2000; **4**(02): 183-213.

[27] OpenSees Wiki: Steel02 Material -- Giuffré-Menegotto-Pinto Model with Isotropic Strain Hardening. http://opensees.berkeley.edu/wiki/index.php/Steel02_Material_--_Giuffr%C3%A9-Menegotto-Pinto_Model_with_Isotropic_Strain_Hardening.

[28] Taucer FF, Spacone E, Filippou FC. A fiber beam-column element for seismic response analysis of reinforced concrete structures. *Report UCB/EERC-91/17*. Earthquake Engineering Research Center, University of California at Berkeley, 1991.

[29] Imbsen and Associates Inc. (2007). XTRACT-Cross Section Analysis Program for Structural Engineers-Step by Step Examples, IMBSEN Software Systems v. 3.0.8, California.

[30] Orakcal K, Wallace JW. Flexural modeling of reinforced concrete walls-experimental verification. *ACI Structural Journal*, 2006, **103**(2): 196-206.

[31] Adebar P, Ibrahim AMM, Bryson M. Test of high-rise core wall: effective stiffness for seismic analysis. *ACI Structural Journal* 2007; **104**(5): 549-559.